Electronic Supplementary Material (ESI) for Dalton Transactions.

Polymorphism in A_3MF_6 (A = Rb, Cs; M = Al, Ga) Grown using Mixed Halide Fluxes

Gregory Morrison,[a] Lakshani W. Masachchi,[a] Hunter B. Tisdale,[a] Tieyan Chang,[b] Virginia G. Jones,[a] K. Pilar Zamorano,[a] Logan S. Breton,[a] Mark D. Smith,[a] Yu-Sheng Chen,[b] Hans-Conrad zur Loye*,[a]

[a]*Department of Chemistry and Biochemistry, University of South Carolina, Columbia, SC, 29208*
[b]*NSF's ChemMatCARS, The University of Chicago, Lemont, IL, 60439*
*Corresponding author. E-mail: zurLoye@mailbox.sc.edu

Comparison of the Two Models for *m*-Cs_3GaF_6

Table S1 compares the crystallographic data for the two models for *m*-Cs_3GaF_6. *m*-Cs_3GaF_6-GM is the model described in the manuscript whereas *m*-Cs_3GaF_6-MDS is the second, independently solved structure. Note that post structure solution, the atoms were renumbered and the origin was shifted to aide in comparison with the original model. Figure S1 highlights the structural differences between the two models. Only two substantial differences exist between the two models, namely, the F atom locations in the disordered Ga(2)F_6 polyhedron are approximated differently and one of the Cs atoms in the original model was modeled as disordered whereas they were all modeled as single positions in the second model. The two differences are discussed below.

The first difference between the two models is how the fluorine atoms in the Ga(2)F_6 polyhedra are modeled. It should be noted that these polyhedra are very disordered and in both cases the modeled fluorine positions are only an approximation of the actual disorder. In *m*-Cs_3GaF_6-GM, the two symmetrically equivalent axial F atoms are modeled as having three positions each and the four symmetrically equivalent equatorial F atoms are also modeled as having three positions each. The occupancies of these positions were refined but constrained to result in three distinct orientations of the Ga(2)F_6 polyhedron, and the F atomic displacement parameters were modeled anisotropically. In *m*-Cs_3GaF_6-MDS, the two symmetrically equivalent axial F atoms are modeled as having four positions each and the four symmetrically equivalent equatorial F atoms are also modeled as having four positions each. The occupancies of these positions are all constrained to 25%, and the F atomic displacement parameters were modeled isotropically.

The second difference between the two models is that *m*-Cs_3GaF_6-GM models the Cs(1) position as disordered across two sites whereas *m*-Cs_3GaF_6-MDS models the Cs(1) as a single, fully occupied position. While modeled as a single position, a residual electron density peak is observed in *m*-Cs_3GaF_6-MDS in the location of the Cs(1b) site in *m*-Cs_3GaF_6-GM. Due to the large size and low charge of Cs and its resulting high ionicity, low bond directionality, and weak bonding, it is extremely common to observe Cs disorder within structures. There are plenty of recent examples of disordered Cs in the literature, both from our group[1-4] and from others.[5-12] In *m*-Cs_3MF_6, disorder in the Cs(1) position is particularly expected as these Cs atoms are adjacent to disordered M(2)F_6 polyhedra. For this reason, we chose to model the Cs(1) position as disordered in the *m*-Cs_3AlF_6 and *m*-Cs_3GaF_6 models included in the manuscript. The Cs(1b) and F(2c) atoms were constrained to have the same occupancy as the other two F(2) sites are too close to Cs(1b) to exist at the same time. Separately refining the Cs(1b) and F(2c) occupancies resulted in respective occupancies of 31.2% and 31.7% for *m*-Cs_3AlF_6 and 31.0% and 31.6% for *m*-Cs_3GaF_6, whereas, constraining the two occupancies led to occupancies of 31.5 % and 31.4 %, respectively. It should be noted that similar magnitude residual electron density peaks exist near other Cs atoms where modelling them would result in physically impossible bond distances and that modelling the Cs(1) position as a single or disordered site had little effect on the refinement statistics.

Table S1. Crystallographic data for SCXRD structure refinements of the reported models.

Compound	*m*-Cs_3GaF_6-GM	*m*-Cs_3GaF_6-MDS
Space group	*C*2/*m*	*C*2/*m*
Pearson Symbol	mC120	mC120
a (Å)	11.3996(3)	11.396(6)
b (Å)	19.7132(4)	19.760(11)
c (Å)	11.4551(4)	11.453(6)
β (º)	109.7000(10)	109.72(2)
V (Å^3)	2423.55(12)	2428(2)
Z	12	12
Crystal size (mm^3)	0.04 x 0.04 x 0.04	0.06 x 0.03 x 0.02
Temperature (K)	300(2)	301(2)
Density (g cm^{-3})	4.789	4.780
θ Range (°)	2.161 – 33.137	1.889 – 30.027
μ (mm^{-1})	16.760	16.730
Data Collection and Refinement		
Collected reflections	102291	82746
Unique reflections	4759	3663
R_{int}	0.0376	0.0487
h	$-17 \leq h \leq 17$	$-16 \leq h \leq 16$
k	$-30 \leq k \leq 30$	$-27 \leq k \leq 27$
l	$-17 \leq l \leq 17$	$-16 \leq l \leq 16$
$\Delta\rho_{max}$ (e Å^{-3})	4.065	3.399
$\Delta\rho_{min}$ (e Å^{-3})	-3.099	-2.781
GoF	1.159	1.154
Extinction coefficient	0.000159(14)	-
[a] $R_1(F)$ for $F_o^2 > 2\sigma(F_o^2)$	0.0281	0.0278
[b] $R_w(F_o^2)$	0.0717	0.0675

[a] $R_1 = \Sigma||F_0| - |F_c||/\Sigma|F_0|$

[b] $wR_2 = [\Sigma w(F_o^2 - F_c^2)^2/\Sigma w(F_0^2)^2]^{1/2}$; $P = (F_o^2 + 2F_c^2)/3$; $w = 1/[\sigma^2(F_o^2) + (0.0291P)^2 + 25.0230P]$ for *m*-Cs_3GaF_6; $w = 1/[\sigma^2(F_o^2) + (0.0238P)^2 + 33.5978P]$ for *m*-Cs_3GaF_6-MDS.

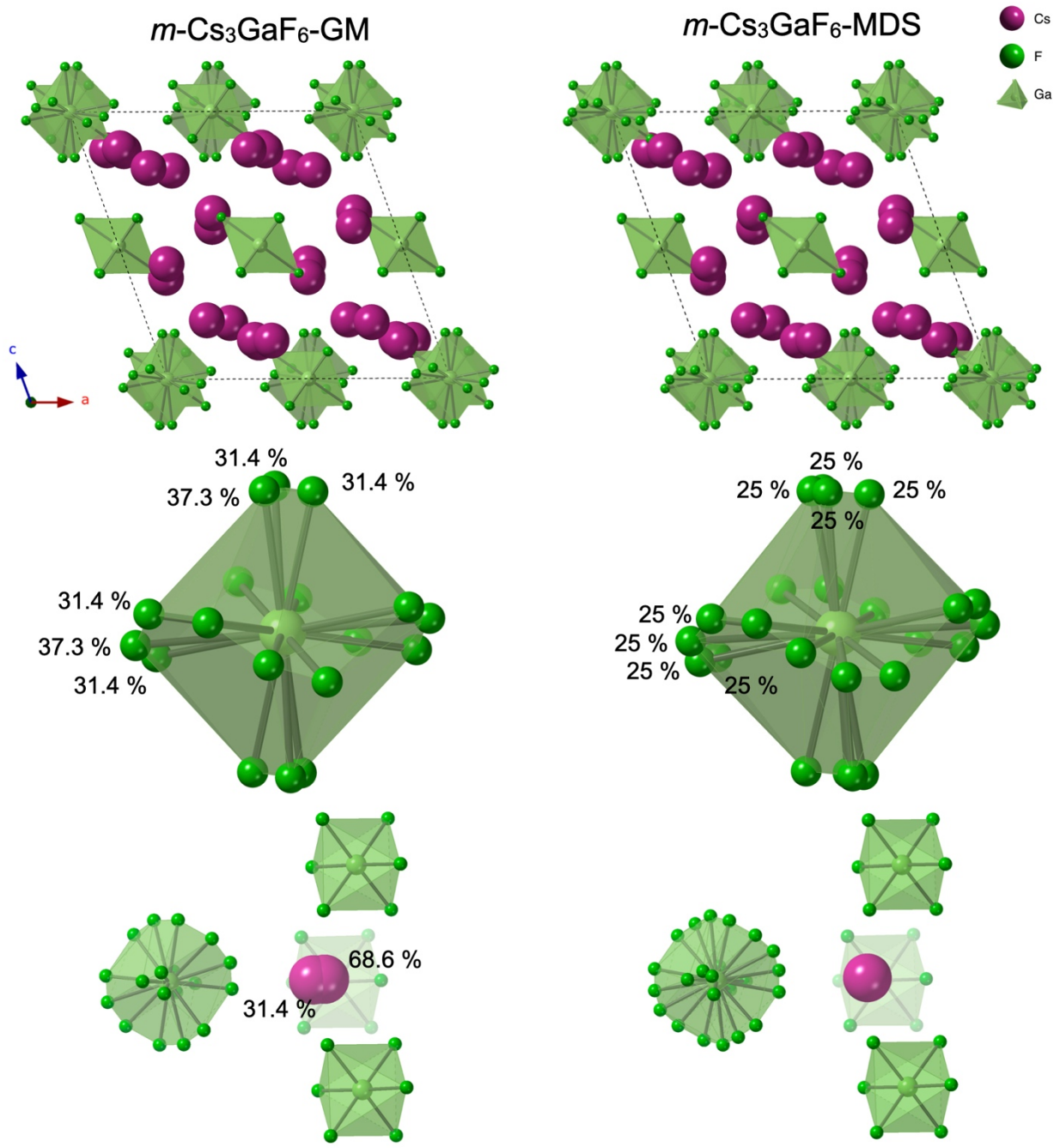

Figure S1. Comparison of the two structure models for *m*-Cs_3GaF_6, showing (top) a view down the *b*-direction, (middle) the disordered Ga(2)F_6 polyhedron, and (bottom) the local environment surrounding the disordered or ordered Cs(1) atom.

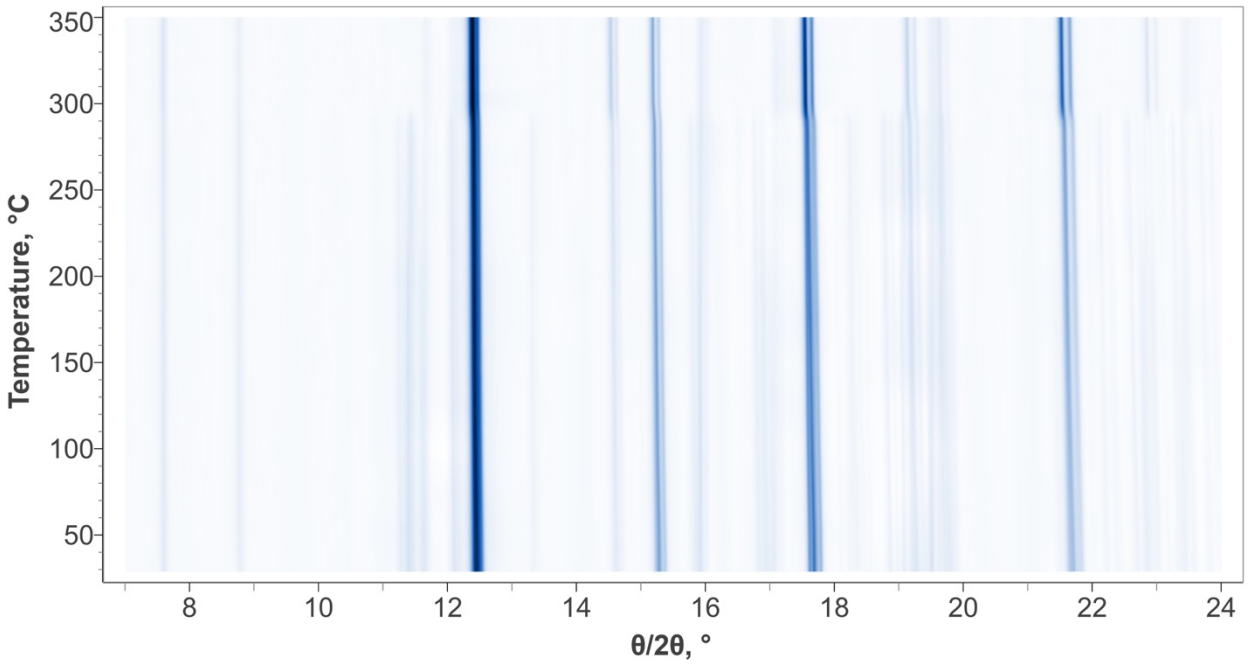

Figure S2. Waterfall plot showing the change in PXRD pattern (Mo K_α) upon heating for Cs_3AlF_6, highlighting the structure transition from *m*-Cs_3AlF_6 to *c*-Cs_3AlF_6 at 291.2 °C.

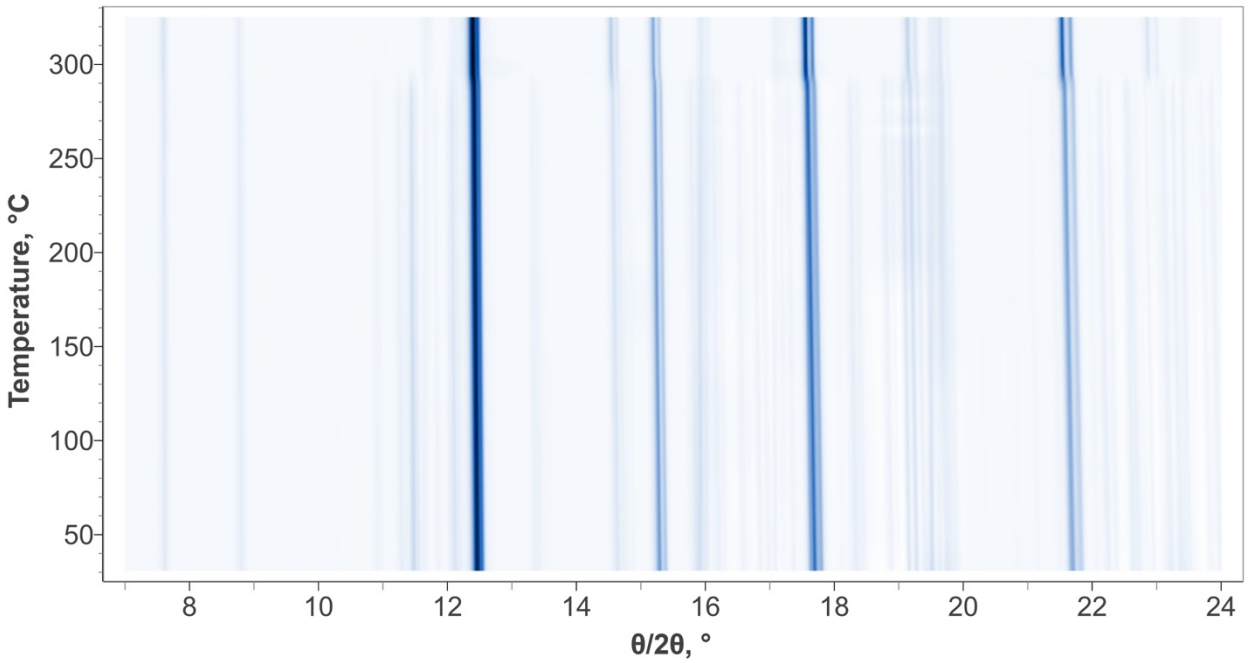

Figure S3. Waterfall plot showing the change in PXRD pattern (Mo K_α) upon cooling for Cs_3AlF_6, highlighting the structure transition from *c*-Cs_3AlF_6 to *o*-Cs_3AlF_6 at 290.0 °C.

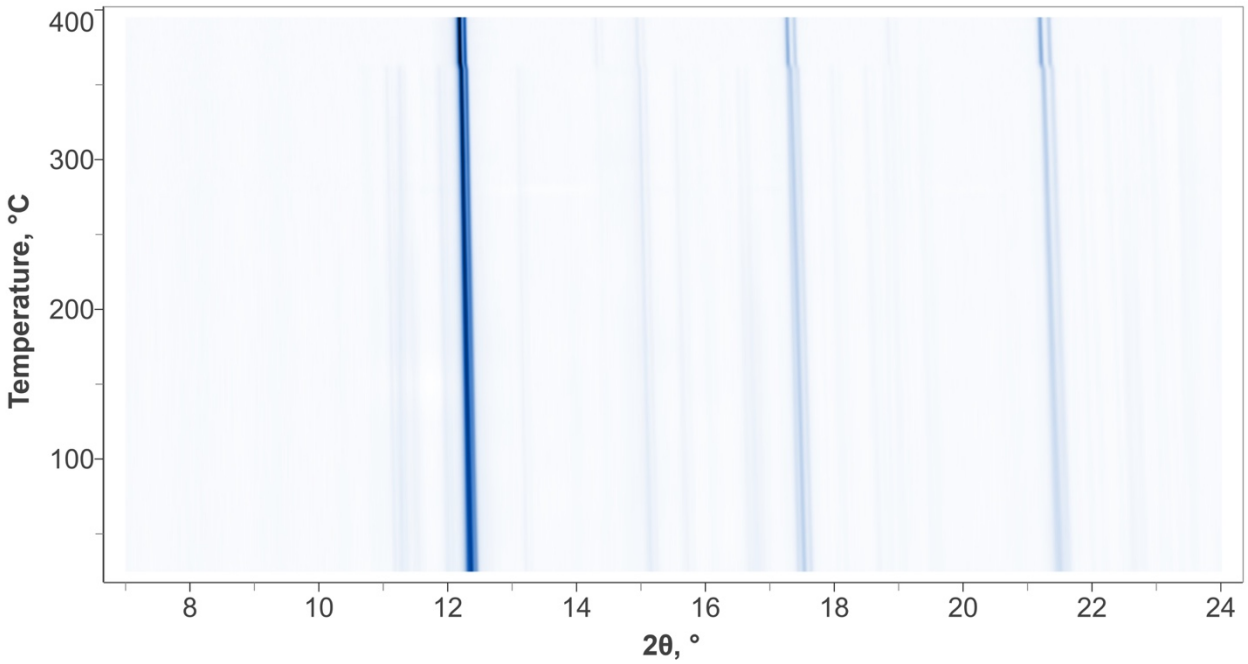

Figure S4. Waterfall plot showing the change in PXRD pattern (Mo K_α) upon heating for Cs_3GaF_6, highlighting the structure transition from *m*-Cs_3GaF_6 to *c*-Cs_3GaF_6 at 367.2 °C.

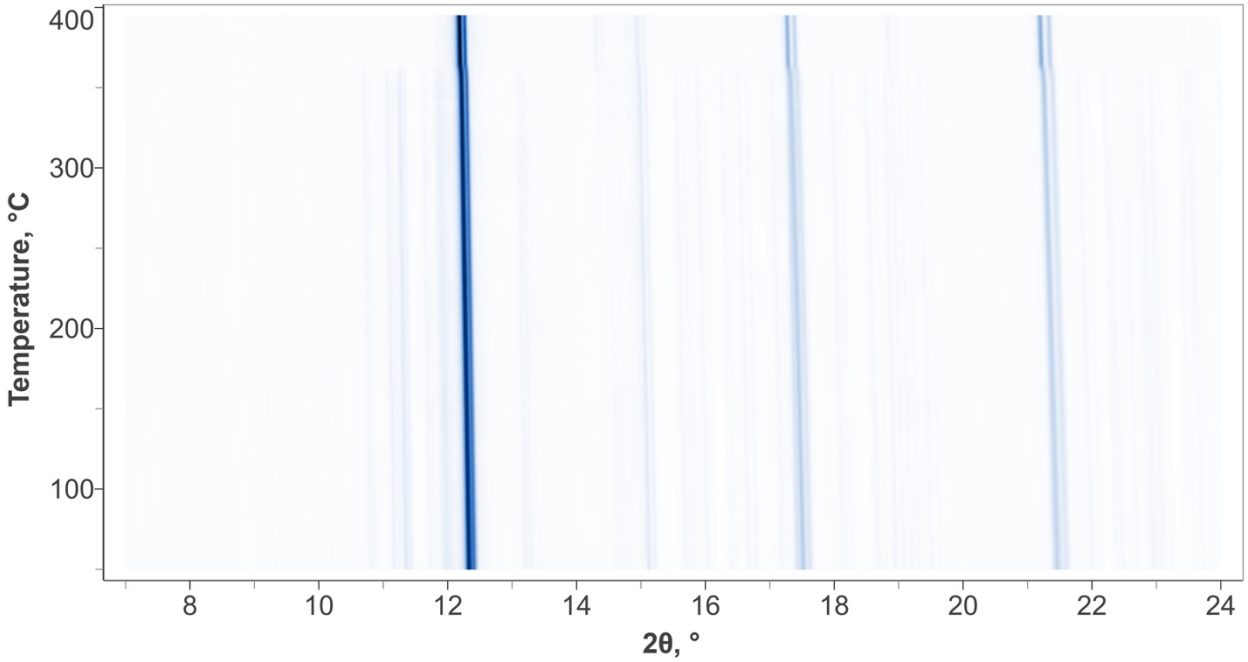

Figure S5. Waterfall plot showing the change in PXRD pattern (Mo K_α) upon cooling for Cs_3GaF_6, highlighting the structure transition from *c*-Cs_3GaF_6 to *o*-Cs_3GaF_6 at 366.5 °C.

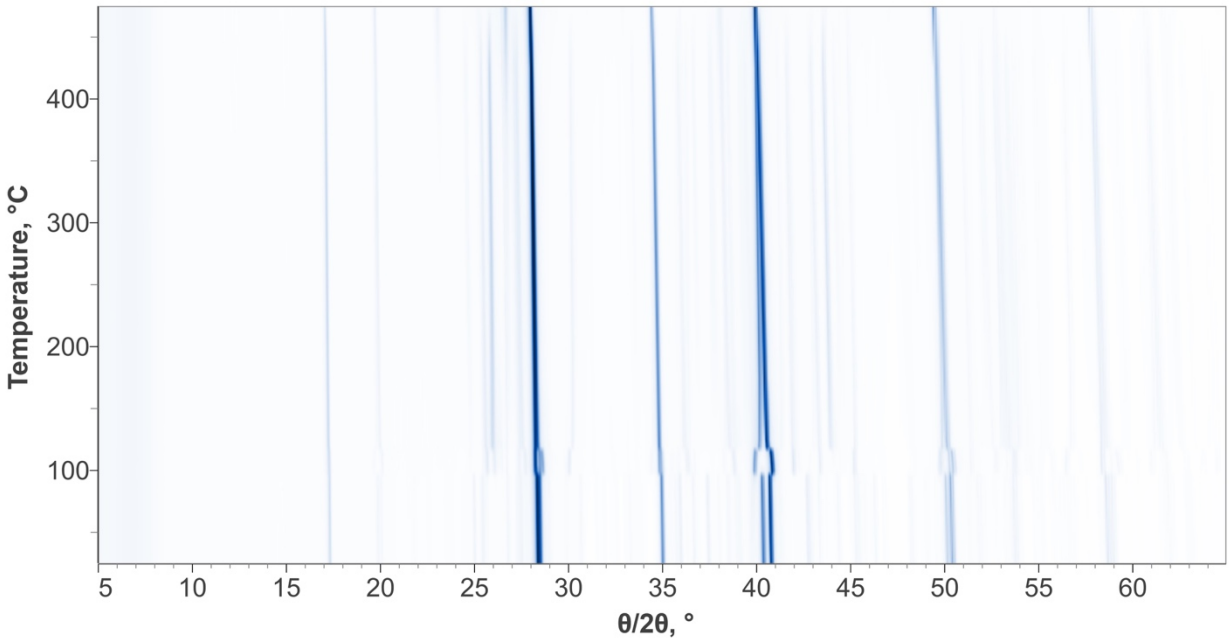

Figure S6. Waterfall plot showing the change in PXRD pattern (Cu K_α) upon heating for Rb_3GaF_6, highlighting the three structure transitions from *t*-Cs_3GaF_6 to two intermediate phases prior to forming *c*-Cs_3GaF_6 at 397.2 °C.

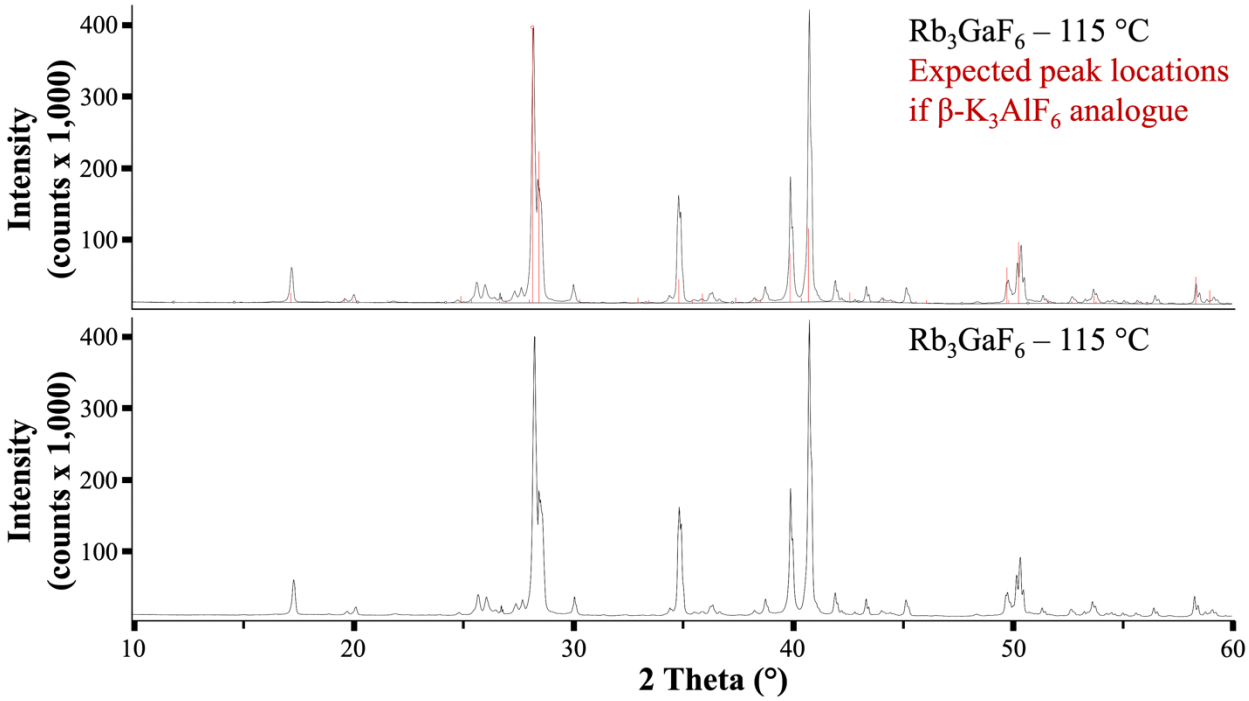

S7. Powder XRD data (Cu K_α) for Rb_3GaF_6 at 115 °C showing (bottom) the experimental data and (top) the experimental data (black) with the expected peak locations if the compound is analogous to β-K_3AlF_6 (red). The powder pattern was calculated using the β-K_3AlF_6 CIF with the K atoms changed to Rb atoms, the Al atoms changed to Ga atoms, and the lattice parameters changed to the best fitting parameters, which were obtained by refinement using the Rigaku SmartLab Studio II software: a = 14.0056(14) Å and c = 9.0358(11) Å.

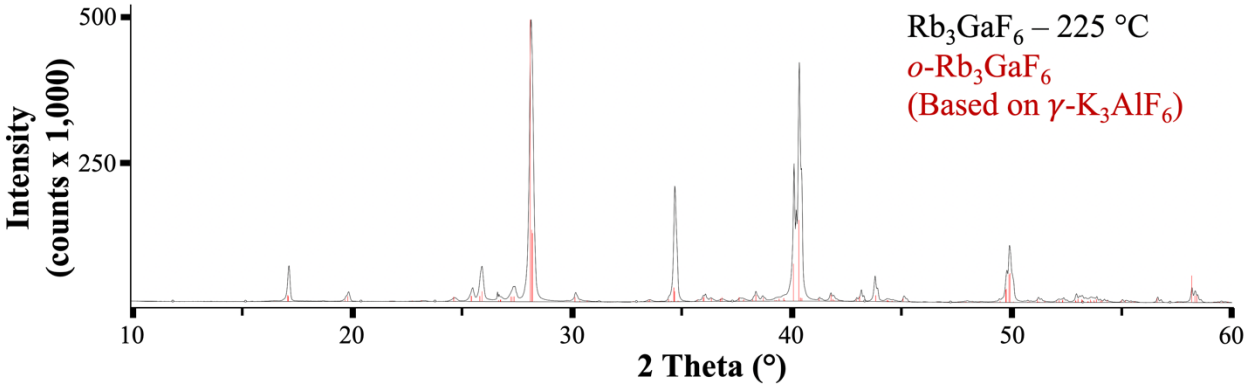

S8. Powder XRD data (Cu K_α) for Rb_3GaF_6 at 225 °C showing the experimental data (black) and pattern calculated based on the γ-K_3AlF_6 CIF (red). The powder pattern was calculated by changing the K atoms to Rb atoms, changing the Al atoms to Ga atoms, and changing the lattice parameters to those obtained by refinement using the Rigaku SmartLab Studio II software: a = 37.959(4) Å, b = 12.6368(12) Å, and c = 17.9872(12) Å.

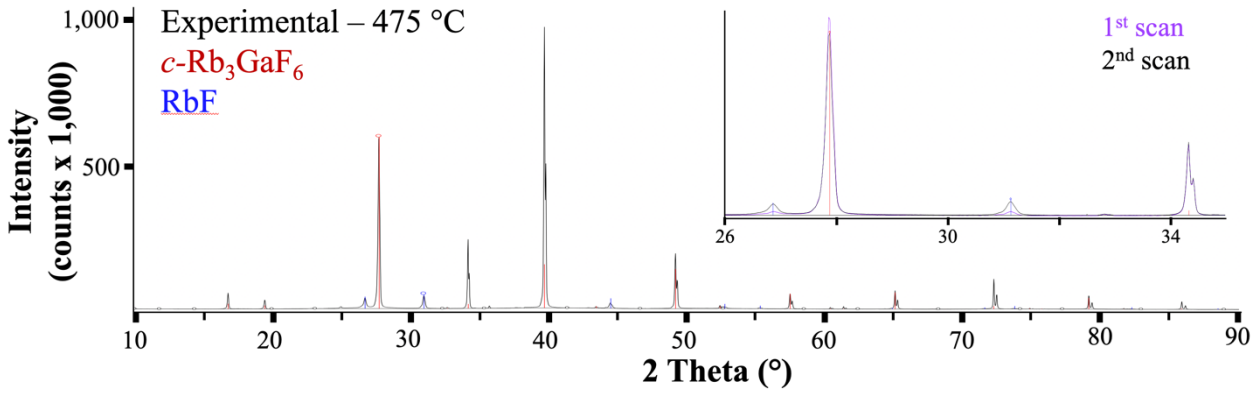

S9. Powder XRD data (Cu K_α) for Rb_3GaF_6 at 475 °C showing the experimental data (black) and pattern calculated from the CIF (red). The inset shows two consecutive scans showing that the extra peaks (identified as RbF) grow in over time. Such sample decomposition was not observed in the TGA.

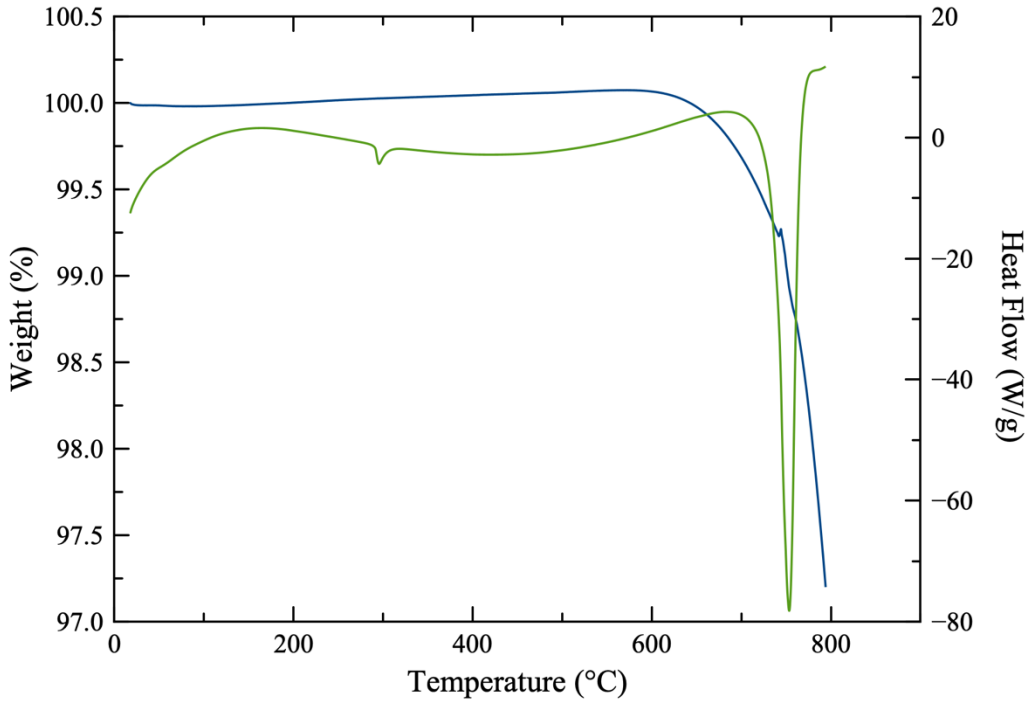

Figure S10. TGA data for Cs_3AlF_6 showing the weight change (blue) and heat flow (green) during heating.

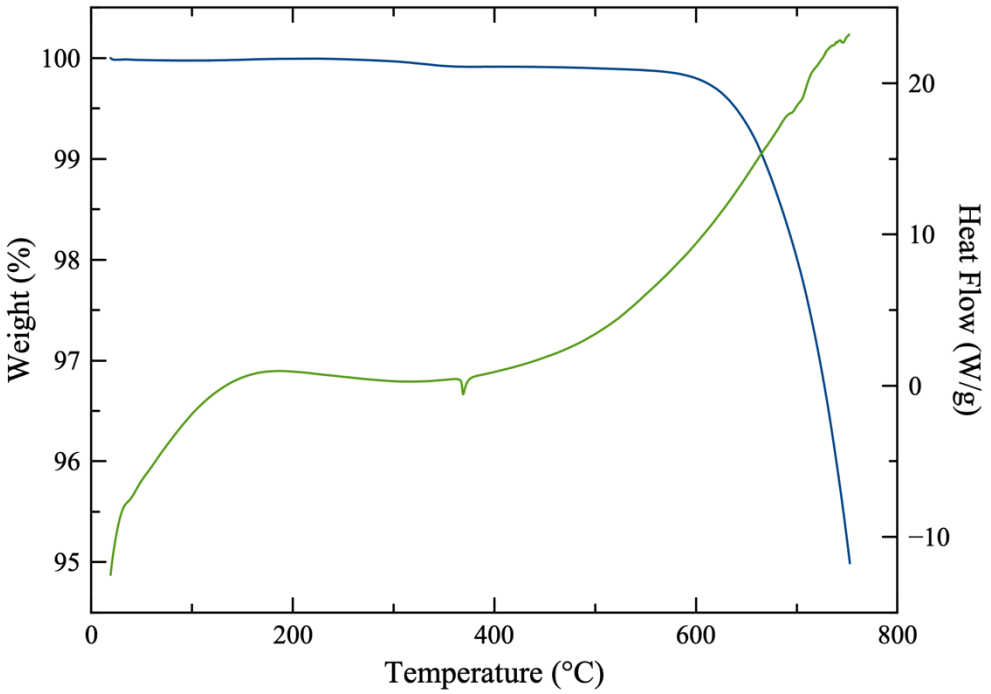

Figure S11. TGA data for Cs_3GaF_6 showing the weight change (blue) and heat flow (green) during heating.

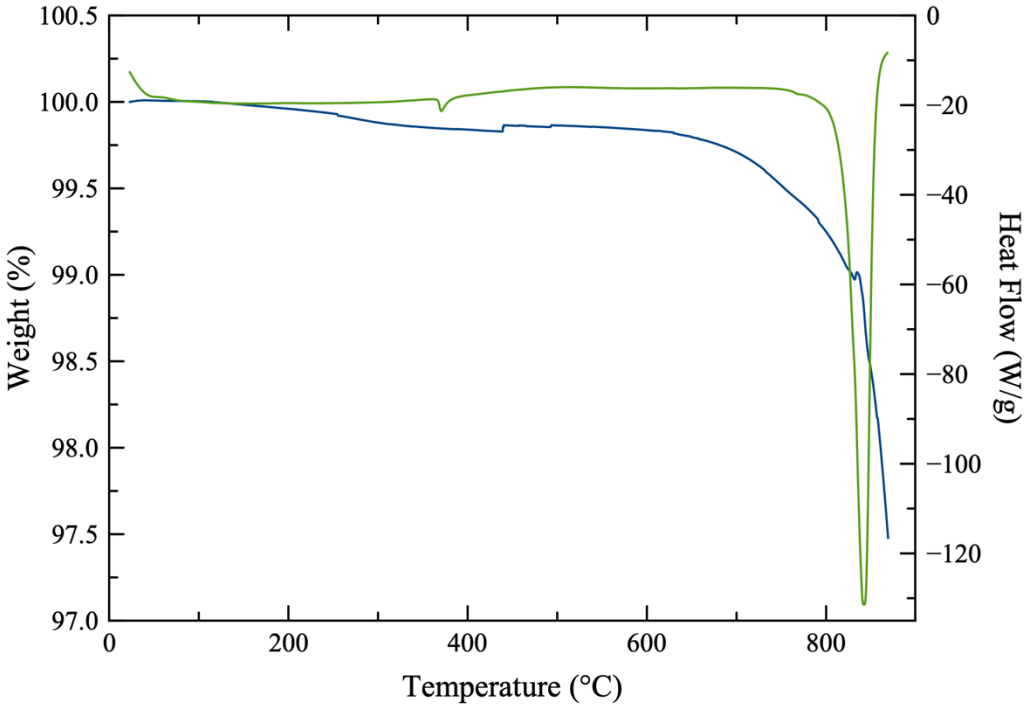

Figure S12. TGA data for Rb_3AlF_6 showing the weight change (blue) and heat flow (green) during heating.

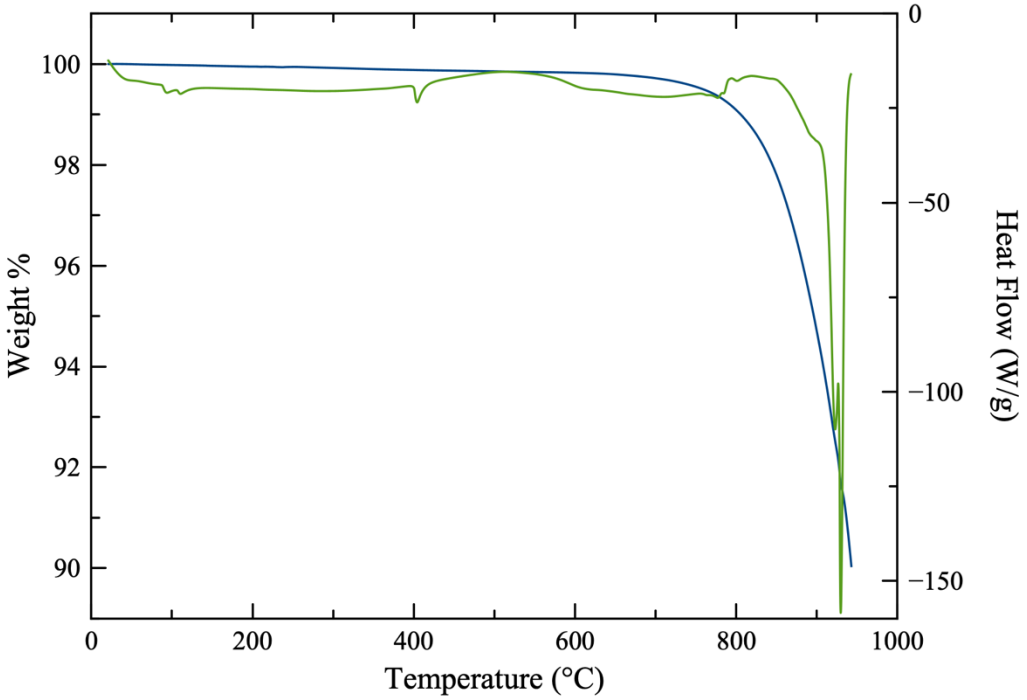

Figure S13. TGA data for Rb_3GaF_6 showing the weight change (blue) and heat flow (green) during heating.

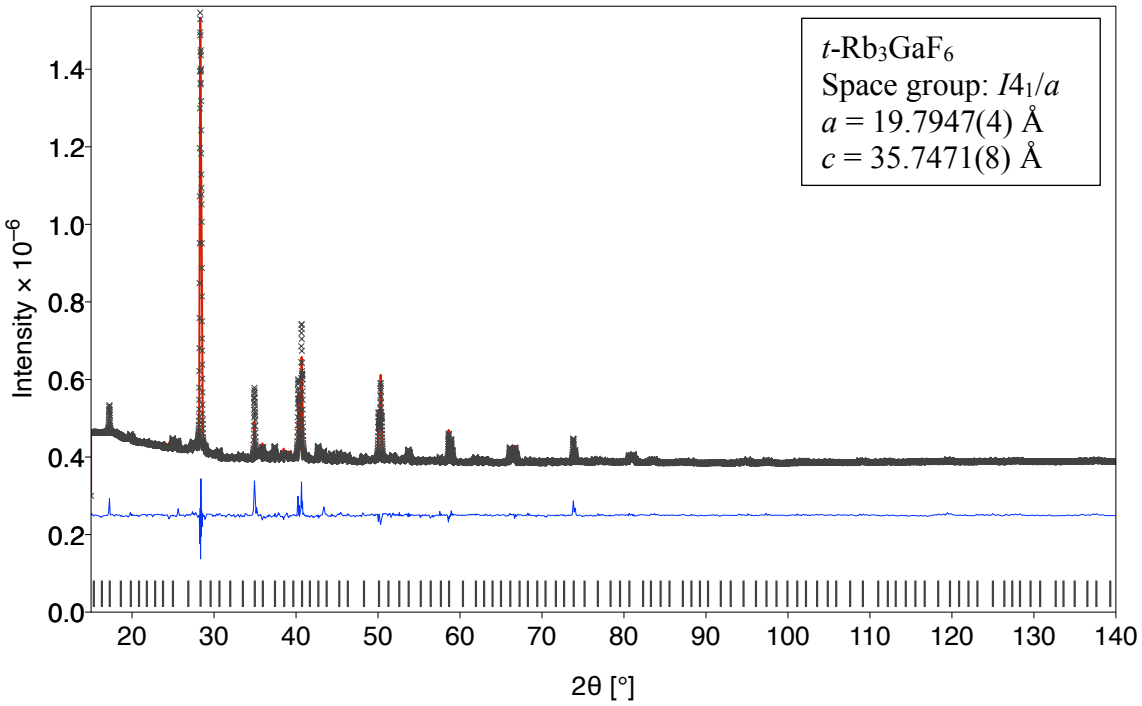

Figure S14: Rietveld refinement plot of Rb_3GaF_6 at room temperature; red line is Rietveld fit, black X's are observed PXRD (Cu K_α), blue line is residual, and vertical black ticks are allowed Bragg reflections.

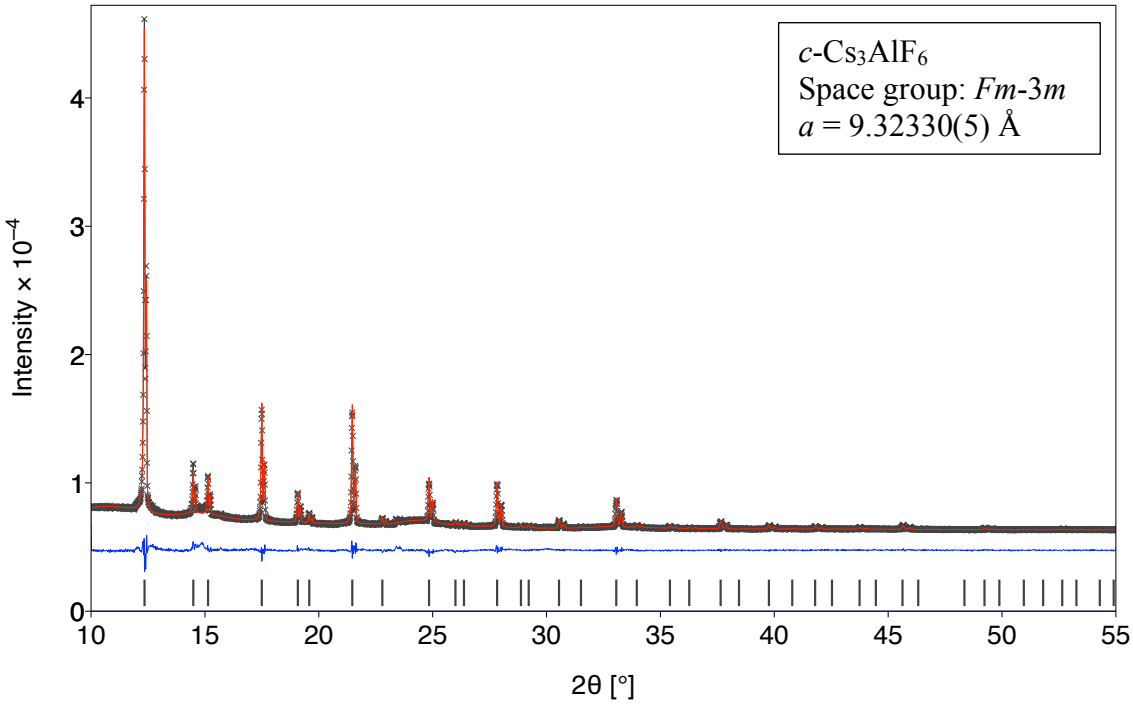

Figure S15: Rietveld refinement plot of Cs_3AlF_6 at 350°C; red line is Rietveld fit, black X's are observed PXRD (Mo K_α), blue line is residual, and vertical black ticks are allowed Bragg reflections.

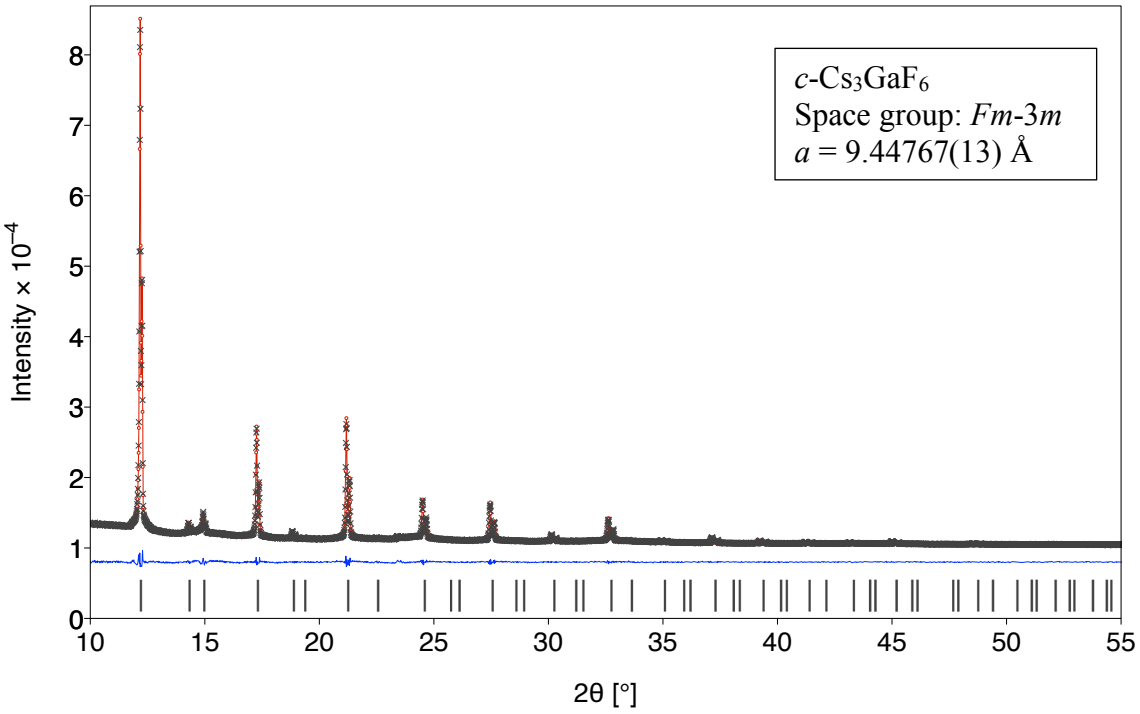

Figure S16: Rietveld refinement plot of Cs_3GaF_6 at 400°C; red line is Rietveld fit, black X's are observed PXRD (Mo K_α), blue line is residual, and vertical black ticks are allowed Bragg reflections.

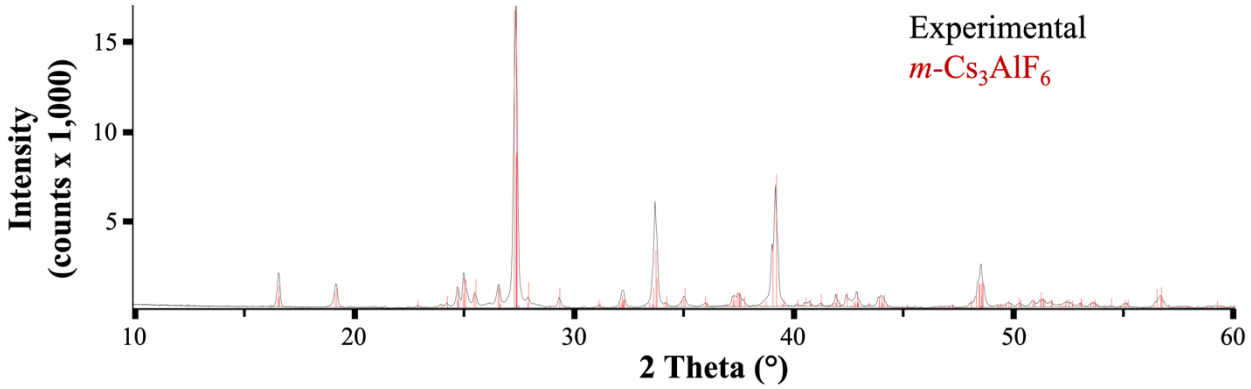

Figure S17. Powder XRD data (Cu K_α) for *m*-Cs_3AlF_6 showing the experimental data (black) and pattern calculated from the CIF (red).

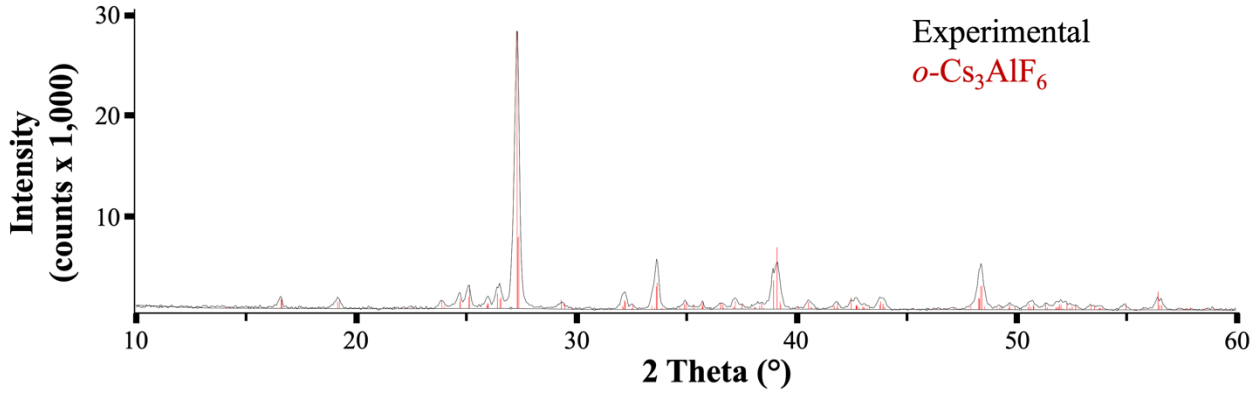

Figure S18. Powder XRD data (Cu K_α) for *o*-Cs_3AlF_6 showing the experimental data (black) and pattern calculated from the CIF (red).

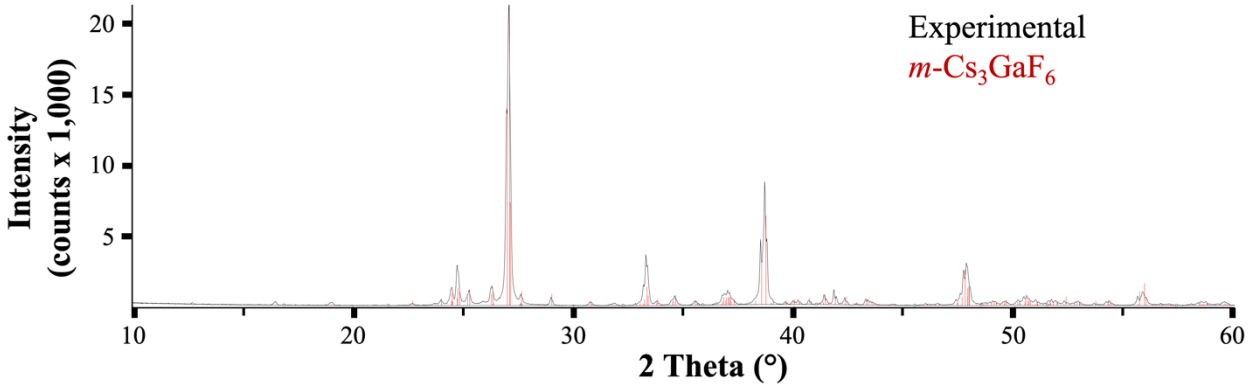

Figure S19. Powder XRD data (Cu K_α) for *m*-Cs_3GaF_6 showing the experimental data (black) and pattern calculated from the CIF (red).

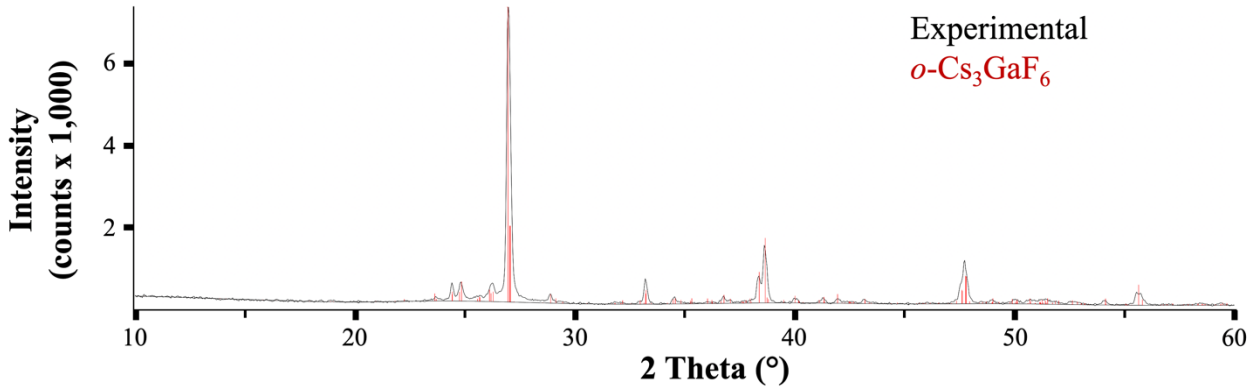

Figure S20. Powder XRD data (Cu K_α) for *o*-Cs_3GaF_6 showing the experimental data (black) and pattern calculated from the CIF (red).

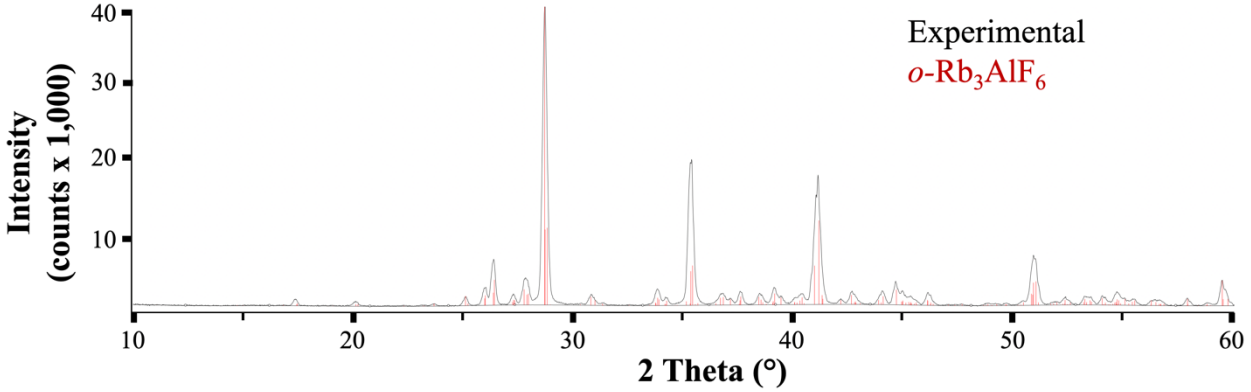

Figure S21. Powder XRD data (Cu K_α) for *o*-Rb_3AlF_6 showing the experimental data (black) and pattern calculated from the CIF (red).

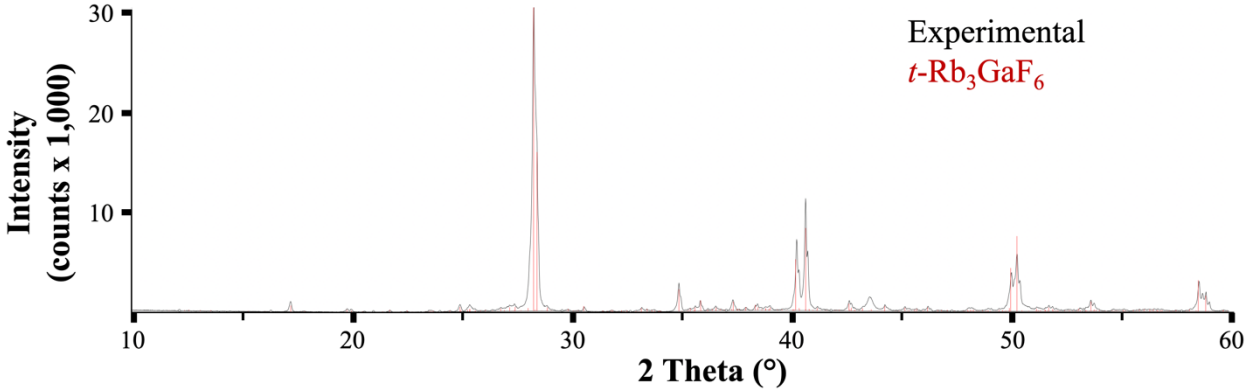

Figure S22. Powder XRD data (Cu K_α) for *t*-Rb_3GaF_6 showing the experimental data (black) and pattern calculated from the CIF (red).